

Temperature gradient driven electron transport in NSTX and Tore Supra

W. Horton¹, H.V. Wong¹, P.J. Morrison¹, A. Wurm¹, J.H. Kim¹,
J.C. Perez¹, J. Pratt¹, G.T. Hoang², B.P. LeBlanc³ and R. Ball⁴

¹ Institute for Fusion Studies, The University of Texas at Austin, Austin, Texas, 78712, USA

² Association Euratom-CEA, CEA/DSM/DRFC, CEA Cadarache, 13108 Saint-Paul-Lez Durance, France

³ Plasma Physics Laboratory, Princeton University, Princeton, NJ 08543, USA

⁴ The Australian National University, Canberra, Australia

Received 10 December 2004, accepted for publication 3 June 2005

Published 9 August 2005

Online at stacks.iop.org/NF/45/976

Abstract

Electron thermal fluxes are derived from the power balance for Tore Supra (TS) and NSTX discharges with centrally deposited fast wave electron heating. Measurements of the electron temperature and density profiles, combined with ray tracing computations of the power absorption profiles, allow detailed interpretation of the thermal flux versus temperature gradient. Evidence supporting the occurrence of electron temperature gradient turbulent transport in the two confinement devices is found. With control of the magnetic rotational transform profile and the heating power, internal transport barriers are created in TS and NSTX discharges. These partial transport barriers are argued to be a universal feature of transport equations in the presence of invariant tori that are intrinsic to non-monotonic rotational transforms in dynamical systems.

PACS numbers: 52.25.Fi, 52.35.Qz, 52.55.Fa

(Some figures in this article are in colour only in the electronic version)

1. Electron transport in tokamaks

Turbulent transport of electron thermal energy appears to be ubiquitous in tokamaks. This suggests that it may arise from the small space and time scales associated with electron temperature gradient (ETG) driven drift wave turbulence. Simulations show that, while the source of the turbulence is on the scale of the electron gyroradius ρ_e , the nonlinear saturated states have large-scale structures on the scale of the collisionless skin depth. Various numerical simulations with two-component fluids, gyrofluids and gyrokinetics show levels of electron diffusivity comparable to that of the ion thermal transport from ion temperature gradient (ITG) driven turbulence. These results support the general conclusion of Kadomtsev [1] that there is an intrinsic level of anomalous electron turbulent transport in toroidal confinement devices. For higher values of $\beta_e = 2\mu_0 p_e / B^2$ and not too low plasma density, the characteristic scale length is the collisionless skin depth $\delta_s = c/\omega_{pe}$, owing to the intrinsic inductive electric field from the magnetic fluctuations.

The time scale of relevance is that for the microscale electron dynamics $\tau_e = R/v_e$. Particular theoretical formulae, developed for the electron thermal fluxes with critical gradients, have successfully interpreted transport in

Tore Supra (TS) with fast wave electron heating, where thermal fluxes and gradients vary over an order of magnitude in response to radio frequency (RF) power increasing from 0.7 to 7.5 MW [2–4]. These are high β_e , helium discharges with 0.65 MA/2.2 T in a classic tokamak geometry with $R/a = 2.2\text{ m}/0.7\text{ m}$.

An example for TS is shown in figure 1(a) using the integrated CRONOS transport code [5], with the ETG transport model for a stair-stepped fast wave heating profile of 3 and 6 MW. This TS discharge (#18368) has $I_p = 0.65\text{ MA}$, $B = 2.2\text{ T}$, $n_e(0) = 4 \times 10^{19}\text{ m}^{-3}$ and $T_e(0) = 4\text{ keV}$ with the fast wave power rising from 3 to 6 MW. The time evolution of the electron temperature $T_e(r, t)$ at various radii, the electron energy content $W_e = \frac{3}{2} \int p_e d^3x$, the loop voltage $V_1(t)$ and the Faraday rotation angles are all shown in figure 1. In figure 1 the dashed curves are the measured and inferred values while the solid curves are derived from the CRONOS code simulation with the ETG mode. In the CRONOS code simulations shown the edge electron temperature is fixed as a boundary condition taken from the experimental data and only the electron diffusivity is taken from three models for making the comparisons.

The electron transport formulae derived in Horton *et al* [4] for TS were applied to NSTX for similar plasma conditions, but

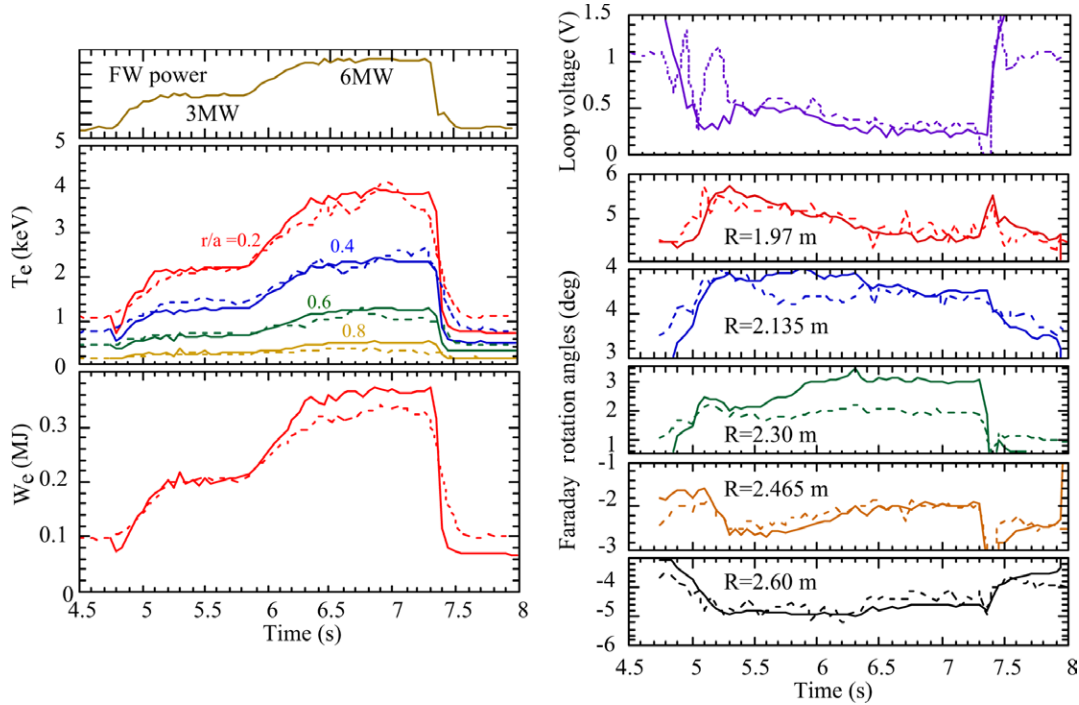


Figure 1. TS FWEH discharge #18368 data (---) compared with the ETG model (—). Top right panel shows the modelled loop voltage (—) versus the measured voltage (---). Lower right panels give the poloidal magnetic field measured (---) and predicted (—) from the Faraday rotation diagnostics and simulation at four vertical cords.

strongly different geometry [6] with small aspect ratio. For the low-aspect ratio $R/a = 0.85 \text{ m}/0.68 \text{ m}$ of NSTX, the fraction of trapped electrons reaches 90% in the outer regions so that the trapped electron mode (TEM) instability is potentially a stronger transport mechanism than the ETG mode. Thus, we analyse high harmonic fast wave (HHFW) heated deuterium and helium discharges with the ETG and TEM thermal flux formulae. A wide range of diagnostics [6] is processed by the TRANSP code and an RF power deposition code to obtain information for the electron transport analysis presented here. We do not have CRONOS runs for the NSTX data.

As in TS, the magnetic shear profile is a critical element in the transport behaviour in NSTX, while toroidal plasma rotation is negligible in the RF driven plasmas. A HHFW NSTX discharge with RF power at 2.5 MW delivered to the core electrons is shown in figure 2 (for discharge #106194). The data is plotted against the square root of the normalized poloidal field, scaled to NSTX's nominal minor radius of 68 cm. This procedure, although not entirely true to real space, reproduces the relevant profile features. Electron power balance analysis gives the thermal flux in figure 2(c), and the thermal diffusivity is seen to increase with radius in figure 2(d).

In TS [7] and NSTX [6], reversed magnetic shear appears to partially block the transport of electron guiding centres. In the rendering of iterates of a discrete map model for drift wave transport this phenomenon corresponds to the formation of shearless invariant tori. An understanding of the persistence of such transport barriers under weak magnetic shear and, in particular, weak reversed shear can be gained by considering low order resonances in the drift wave model [8]. (See [9], where the basic ideas are investigated in the closely analogous context of Rossby waves in a shear flow.)

The destruction of a toroidal barrier between two resonances occurs when perturbations increase to the point where resonances overlap. The lowest order resonances are usually the largest, and hence their effect on transport is dominant. The farther the barrier is away from low order resonances, the more robust it is. This idea can be quantified in terms of number theoretical properties of the rotation number (q -profile) of the barrier: the more irrational the number, the harder it is to approximate by rational numbers because it lies further away from low order resonances [10]. The effect of an almost flat q -profile is to reduce the density of resonances, i.e. the distance between the main resonances is large and therefore small perturbations will not result in overlap [11].

In the reversed shear case, the barrier at q_{\min} , the shearless invariant torus, lies in a region where the density of resonances is very low. In contrast to monotonic q -profiles, resonances exist in pairs in reversed shear regions on opposite sides of q_{\min} . In addition to resonance overlap on each side of the barrier, the new phenomenon of separatrix reconnection between resonance pairs occurs, which for perturbations that are not too large, results in the creation of a *new* transport barrier outside of the resonances after the destruction of the central barrier. We illustrate this mechanism in figure 3. The upper row displays sketches of the poloidal plane with the vertical axis representing the radial coordinate and the horizontal axis the poloidal angle. This row shows two island chains close to the central barrier as they undergo reconnection under the change of q_{\min} . The lower row of the figure displays the rotation number versus the radial coordinate along two lines (labelled s_1 and s_3). Before reconnection (figure 3(a)), a central barrier exists between the resonances, a barrier that is destroyed at the reconnection threshold (figure 3(b)). Afterwards, new

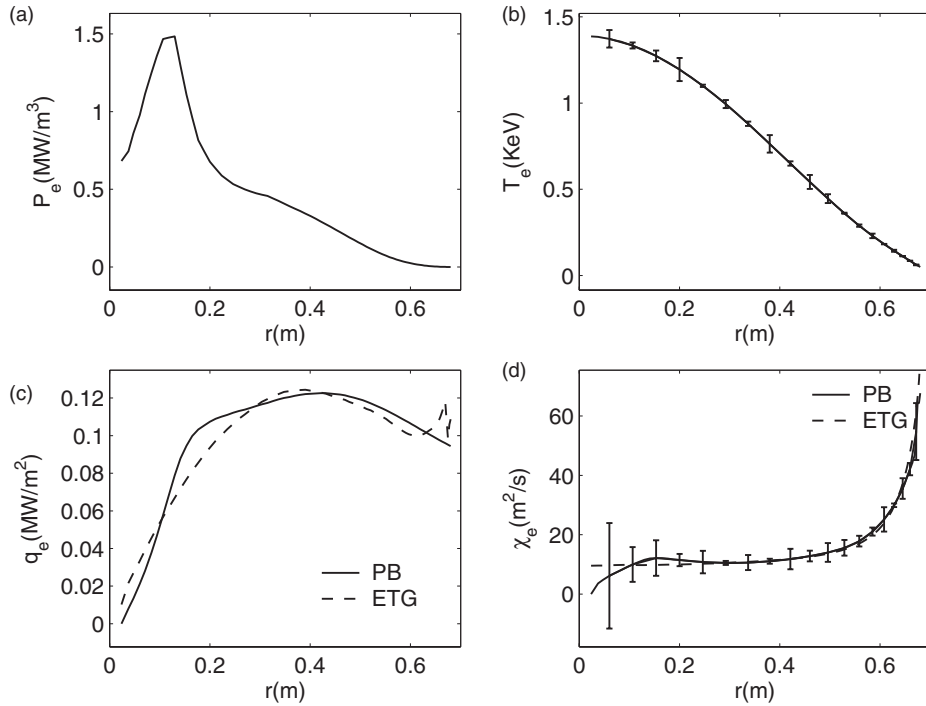


Figure 2. NSTX profiles and power balance analysis for discharge #106194. Frame (a) is the electron absorbed rf power density, (b) the 20 cord 17 ms Thomson scattering electron temperature profile with a 3% random error added to estimate the uncertainty in the electron power balance analysis, (c) the electron thermal fluxes, q_e from power balance and from the ETG model (d) the respective thermal diffusivities with the error estimate for the power balance diffusivity.

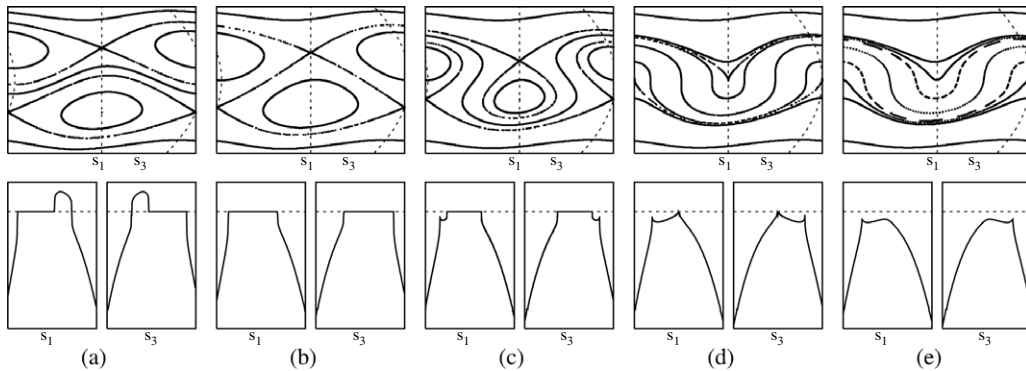


Figure 3. Sketch of reconnection of island chains close to the central barrier at q_{\min} . The upper row depicts the poloidal plane with the vertical axis representing the radial coordinate; the lower row depicts the rotation number versus the radial axis along two lines (labelled s_1 and s_3) (from [12]).

barriers appear that persist throughout the destruction of the island chains (figures 3(c)–(e)).

If the magnetic field line stochasticity on both sides of q_{\min} is very strong (corresponding to large perturbations in the map model), reconnection leads to a loss of electron confinement, as depicted in figure 4. Before reconnection (left picture), initial conditions below the barrier (green) do not mix with initial conditions above (blue). After reconnection, the remnants of the shearless torus (red) act as partial transport barriers. The details of this scenario are actively under investigation. (For some related work see, e.g. [15, 16].) The detailed description of the break-up of shearless invariant tori is a universal phenomenon that depends on the stability of resonances to all orders, an analysis that requires renormalization group techniques [13].

For optimized deuterium HHFW discharges (figure 5) in a regime of weakly reversed magnetic shear, the internal transport barrier (ITB), indicated by the change in the gradient of T_e at $r \approx 0.4$ m, reorganizes inside $r_{\text{ITB}} = 0.4$ m and the χ_e drops to $2\text{--}3$ $\text{m}^2 \text{s}^{-1}$. The q -profile has been obtained from TRANSP analysis [18]. This mode of operation is conducive to a centrally peaked T_e profile nearing 4 keV, with an inflection point (foot) around $r = 0.4$ m (figure 5(b)). Here the reversed magnetic shear reduces the ETG growth rate and changes the topology of the electron guiding centre phase space. Surface of section plots of the electron guiding centres show the formation of shearless invariant tori in the associated poloidal surface of section. Correlated with this improved electron confinement is the accumulation of impurity ions and a rise in the axially-peaked Z_{eff} from 2.8 to 3.8.

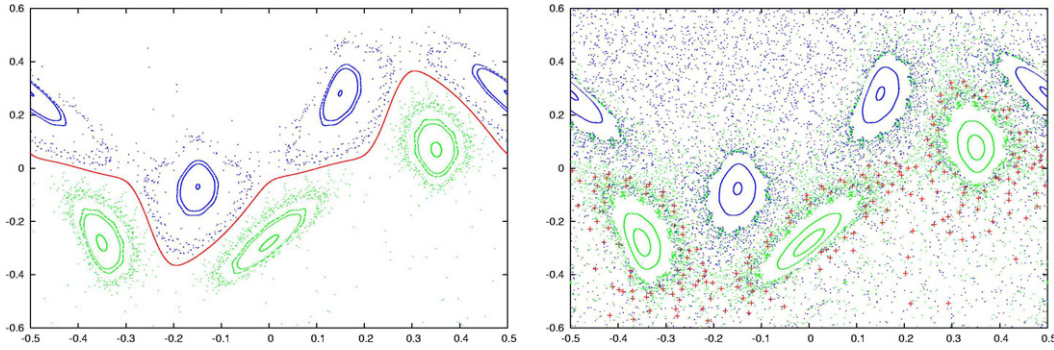


Figure 4. Plots of map model close to q_{\min} for strong field line stochasticity. Before reconnection (left) and after reconnection (right). After reconnection, initial conditions below the barrier (green) mix with those above (blue), but remnants of the shearless torus (red) act as partial barriers (from [14]).

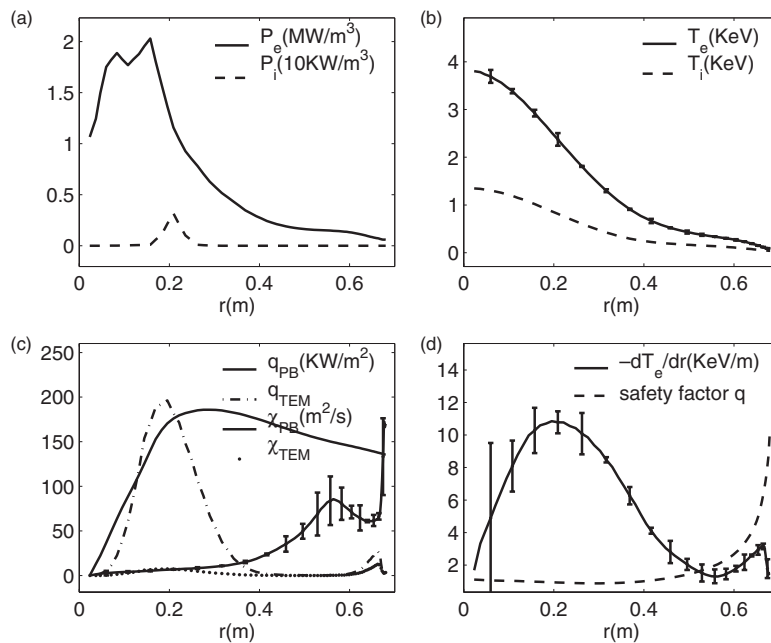


Figure 5. NSTX profiles for reversed magnetic shear discharge #105830 driven by harmonic fast wave RF heating. (a) Deposited power density P_e , P_i into electrons and ions, respectively. (b) Electron and ion temperature profile with a 3% random error only on the electron temperature profile. (c) Electron thermal fluxes, q_{PB} derived from the power balance and q_{TEM} from the trapped electron mode with the associated electron diffusivity χ_{PB} and χ_{TEM} . For q_{PB} , the error bars are given from the profile T_e . (d) The ETGs with error bars from T_e with the safety factor q -profile showing the weakly reversed magnetic shear.

The combination of the low-aspect ratio NSTX and the high-aspect ratio TS classic circular cross-section tokamak, both with high-power fast wave electron heating, is an ideal comparison for electron transport research. The fact that the ETG model is able to explain the electron power balance heat flux in both of these machines is strong evidence for the validity of the model.

The NSTX and TS tokamaks provide data with a wide range of values for key parameters: the temperature ratio T_i/T_e , the aspect ratio R/a , the trapped electron fraction δn_e on a magnetic surface, the electron collisionality $\nu_{*e} = \nu_e q R / v_e \delta^3$, the gradient parameters η_i and η_e , the plasma pressure β_e , the magnetic safety factor q and the shear $s = r q' / q$. Both have high-power auxiliary FW heated plasmas, with 90% of the RF power (3 MW into 4–5 m³ for NSTX and 7 MW in 6 m³ for TS) giving a clear electron power balance channel for the study of the anomalous electron thermal flux q_e (MW m⁻²).

Both tokamaks show a rapid increase of T_{e0} and ∇T_e up to 12 keV m⁻¹ for this similar level of core RF power per electron. The NSTX discharge #106194 with He working gas, has an L-mode edge and with a peaked density profile, has an H-mode-like global confinement time of 30 ms with $H_{97L} \sim 2$. Tore Supra also has peaked density profiles with $H_{97L} \sim 1.7$ in L-mode He plasmas. Figure 5 shows that an optimized 2.15 MW NSTX discharge (#105830) with reversed q -profile that produces an internal electron transport barrier at $R_{ITB}/R_0 = 1.4\text{ m}/1.0\text{ m}$, lasting for about $4\tau_E$ until the peaked ($T_{e0} = 4\text{ keV}$) electron profile collapses from a magnetic reconnection event.

2. Turbulent transport models, ETG and TEM

Stability calculations suggest that the trapped electron mode (TEM), where for example 50–90% of the electrons are

trapped in NSTX beyond $R/R_0 > 1.3$, produces the large anomalous χ_e . In the core region the electron transport is lower, it being driven by the electromagnetic ETG transport in the high $\beta_e \sim 10\%$ collisionless core plasma. In the core region, the magnetic geometry and the plasma conditions are similar to TS where extensive parametric studies over a 40-discharge database confirm the presence of a heat flux described by $q_e = -n_e \chi_e [\nabla T_e - (\nabla T_e)_c]$, with a collisionless skin depth scaling of $\chi_e^{\text{ETG}} \sim T_e^{1/2}/n_e$ and a linear theory value of the critical gradient $(\nabla T_e)_c$ [2–4]. Cross polarization scattering data indicates that there is a significant level of small scale magnetic turbulence in the core plasma that increases with $[\nabla T_e - \nabla T_{e,c}]$ [25].

2.1. Electron temperature gradient

The source of the ETG turbulence is the high-power density, P_{rf} , deposited in the core of the NSTX plasma by HHFW heating. We focus on discharge #106194, with $P_{\text{rf}} = \int d^3x p_{\text{rf}} = V \bar{P}_{\text{rf}} = 3.3 \text{ MW}$ deposited into the core plasma volume $V = 3\text{--}4 \text{ m}^3$. The total plasma volume is $V_T = 11 \text{ m}^3$.

The local electron power balance equation is

$$\frac{\partial}{\partial t} \left(\frac{3}{2} n T_e \right) + \nabla \cdot \left(\frac{3}{2} n T_e \mathbf{v} + \mathbf{q} \right) + n T_e \nabla \cdot \mathbf{v} = p_{\text{rf}} - p_{\text{edge}}, \quad (1)$$

where the RF power per unit volume is $p_{\text{rf}}(r) \approx p_{\text{rf}}^{(0)} e^{-r/L_{\text{rf}}}$ and p_{edge} rises across the last closed flux surface. Assuming the particle sources are zero in the discharge, so that

$$\frac{\partial n}{\partial t} + \nabla \cdot (n \mathbf{v}) = 0, \quad (2)$$

$$m_e n_e \frac{d}{dt} v_{\parallel e} = -en E_{\parallel} - \nabla_{\parallel} p_e + \frac{m_e v_e}{e} j_{\parallel},$$

we obtain three partial differential equations governing the electron turbulence. We separate $T_e = T_{e0} + \delta T_e$ and introduce the dimensionless variables $\delta T_e / T_{e0} = (\rho_e / R) \delta \hat{T}_e$, $e\varphi / T_e = (\rho_e / R) \hat{\varphi}$, $A_{\parallel} / B_z \rho_e = (\rho_e / R) A$, where $\rho_e = m_e v_e / eB$ and $v_e = \sqrt{T_e / m_e}$, and obtain

$$\begin{aligned} \mathbf{v}_E &= \frac{1}{B} \mathbf{e}_z \times \nabla \varphi = \frac{\rho_e v_e}{R} \mathbf{e}_z \times \nabla \hat{\varphi}, \\ \mathbf{q}_e &= \left\langle \frac{3}{2} n T_e \mathbf{v} \right\rangle = -\frac{3}{2} n_e v_e T_e R \left(\frac{\rho_e}{R} \right)^2 \left\langle \delta \hat{T}_e \frac{\partial \hat{\varphi}}{\partial y} \right\rangle. \end{aligned} \quad (3)$$

The isotropic ETG model, we consider here, is given by the following set of three coupled PDEs

$$\begin{aligned} (1 - \nabla_{\perp}^2) \frac{\partial \hat{\varphi}}{\partial t} &= [1 - 2\epsilon_n + (1 + \eta_e) \nabla_{\perp}^2] \frac{\partial \hat{\varphi}}{\partial y} \\ &+ 2\epsilon_n \frac{\partial \delta \hat{T}_e}{\partial y} + [\hat{\varphi}, \nabla^2 \hat{\varphi}] + \partial_{\parallel}^{nl} \nabla_{\perp}^2 \hat{A} - \mu \nabla^4 \hat{\varphi} \\ \left(\nabla^2 - \frac{\beta}{2} \right) \frac{\partial \hat{A}}{\partial t} &= \frac{\beta}{2} (1 + \eta_e) \frac{\partial \hat{A}}{\partial y} + 2 \partial_{\parallel}^{nl} \hat{\varphi} \\ &- \partial_{\parallel}^{nl} \delta \hat{T}_e - [\hat{\varphi}, \nabla^2 \hat{A}] - \frac{\eta}{\mu_0} \nabla^2 \hat{A} \end{aligned} \quad (4)$$

$$\begin{aligned} \frac{\partial \delta \hat{T}_e}{\partial t} &= S_{\text{rf}}(r) - s_{\text{edge}}(r) - [\eta_e - 4\epsilon_n (\Gamma - 1)] \frac{\partial \hat{\varphi}}{\partial y} \\ &- 2\epsilon_n (2\Gamma - 1) \frac{\partial \delta \hat{T}_e}{\partial y} \\ &- (\Gamma - 1) \partial_{\parallel}^{nl} \nabla^2 \hat{A} - [\hat{\varphi}, \delta \hat{T}_e] + \chi_{\perp} \nabla_{\perp}^2 \delta \hat{T}_e + \chi_{\parallel} (\partial_{\parallel}^{nl})^2 \delta \hat{T}_e, \end{aligned}$$

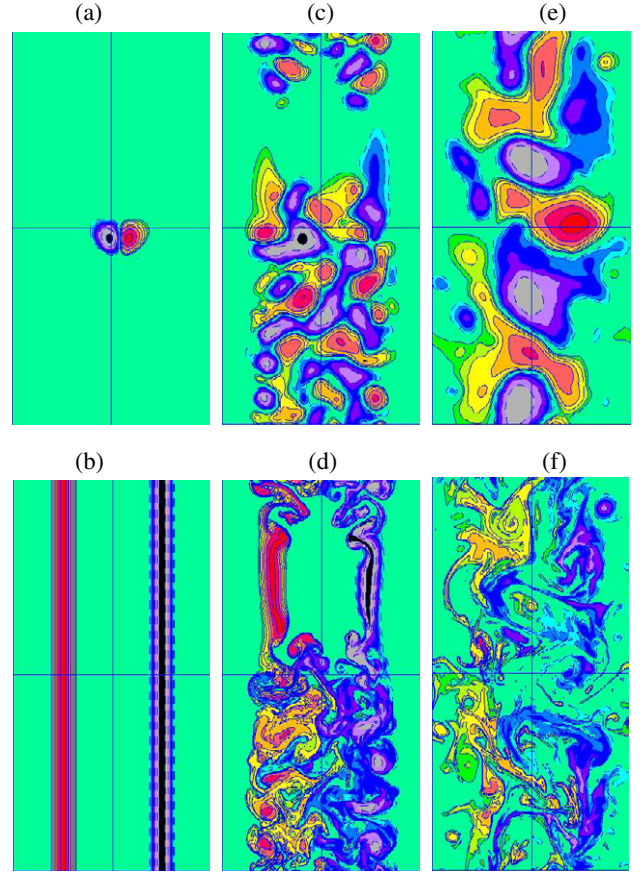


Figure 6. Simulated temperature profiles using equations (4) for early, intermediate and late times. The box size is $40\pi\rho_e \times 80\pi\rho_e$. The top row panels (a), (c) and (e) depict isopotential contours, while the bottom row panel (b), (d) and (f) depict isothermal contours. The magnetic field is out of the page and the horizontal and vertical axes represent the radial and poloidal directions, respectively.

where $\beta = 2\mu_0 p_e / B^2$, $\eta_e = d \ln T_e / d \ln n_e = L_{n_e} / L_{T_e}$ and $\epsilon_n = L_n / R$. The space-time scales used in equation (4) are ρ_e and R/v_e . The dimensionless RF source function is $S_{\text{rf}} = R P_{\text{rf}} / (3/2) (\rho_e / R) n T_e v_e \sim O(1)$ and the sink function is such that $\int d^3x (S_{\text{rf}} - s_{\text{edge}}) = 0$, so that a steady state is reached. For NSTX we have $n T_e \sim 10^4 \text{ Pa}$ and $v_e \rho_e = T_e / B \sim 10^3 \text{ m}^2 \text{ s}^{-1}$. Thus, $(3/2) n T_e v_e \rho_e / R^2 \sim 10^7 \text{ W m}^{-3}$ and $S_{\text{rf}} \sim 0.1$.

We have derived a set of fluid equations more general than equation (4) for the ETG mode with electro pressure anisotropies driven by the LHCD or ECCD. The new complex equations are derived from the kinetic equation for the electron guiding centre distribution function in the small gyroradius limit. For this communication, we have simplified the geometry, taken the limit of an isotropic pressure and used a simple Fick's law for the parallel electron thermal flux to reduce the system to equation (4).

We integrate equations (4) for $\beta = 0.02$, $\epsilon_n = 0.1$ and $\eta_e = 2$ using a pseudospectral method [19,20] on a rectangular grid of $L_x \times L_y = 40\pi\rho_e \times 80\pi\rho_e$. Figure 6 shows the dimensionless electric potential and temperature level surfaces at the intermediate time ($t v_e / R = 100$) and late ($t v_e / R = 180$) time. The isopotential contours in (c) and (e) show the growth of large vortex structures. At the late time the entire plasma

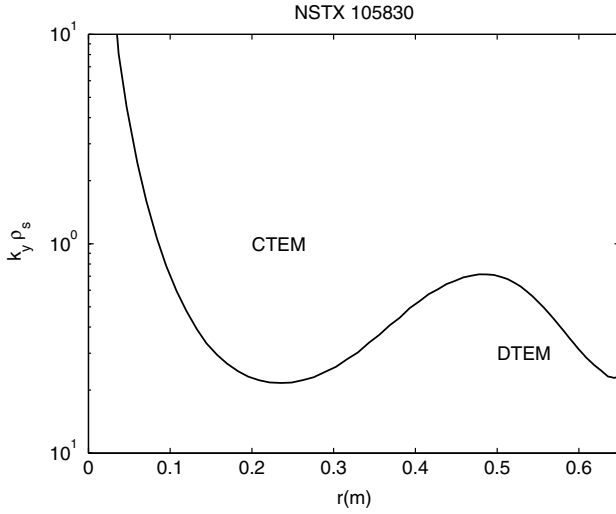


Figure 7. Kadomtsev transition formula from DTEM to CTEM for NSTX. The short wavelength modes above the curve are collisionless (CTEM) and the long wavelength modes below the curve are collisional electron drift modes.

in the region between the source and sink at $x = \pm L_x/4$ is turbulent. The simulation retains the $k_x = 0$ and $k_y = 0$ modes, corresponding to streamers and zonal flows.

Key features of the RF heated-divertor simulation are seen in figure 6. In particular, the intermediate nonlinear phase plots of both the electric potential (figure 6(c)) and temperature (figure 6(d)) show coherent structures mixing the hot and cold regions. The structures formed are like plumes propagating radially with ‘mushroom heads’ in the first stage of the temperature plumes. The scale size of the vortices ranges from 8 to $20\rho_e$ in (figure 6(c)). In the late nonlinear stage, the vortices become large and reach a diameter of $40\rho_e$ or $L_x/3$ (figure 6(e)). In figure 6(f), the temperature field becomes highly filamented and stretches into long thin hot and cold fronts, coexisting with smaller hot and cold, roughly circular, islands. A few of the long filaments extend over the region between the source and the sink.

2.2. Trapped electron mode transport

Electron thermal transport is a by-product of the TEM and is carried by the large pitch angle electrons with density fraction $\delta n_r = n_0\delta$, where $\delta = (B_{\max}/B_{\min})^{1/2} - 1 \approx (2r/R)^{1/2}$ near the axis.

The trapped fraction has $\delta_{\text{NSTX}} \gg \delta_{\text{TS}}$, with $\delta_{\text{NSTX}} = 0.8$ near the outer radii. The Kadomtsev and Pogutse [21] analysis shows that the dissipative TEM is driven by

$$\gamma_k = \frac{\delta^3 \omega_{*e}^2}{\nu_e} = \left(\frac{r}{R}\right)^{3/2} (k_y \rho_s)^2 \left(\frac{c_s^2}{L_n^2 \nu_e}\right) \quad (5)$$

for $\omega_* \delta^{3/2} < \nu_e / \delta^2$ and collisionless (CTEM) growth rate,

$$\gamma_k = \left(\frac{r}{R}\right)^{1/2} (k_y \rho_s) \left(\frac{c_s R}{L_n^2}\right). \quad (6)$$

Figure 7 shows the division of the DTEM and CTEM for NSTX.

This mode is then driven by the density gradient of the trapped particles rather than the temperature. The anomalous diffusivity of the trapped electrons and ions is given by Kadomtsev and Pogutse as

$$D_t = c_{\text{TEM}} D_{gB} \left(\frac{c_s R}{\nu_e L_n^2}\right) \quad (7)$$

and the associated electron thermal transport can be either inwards or outwards depending on the values of ν_{*e} and η_e . At low collisionality the electron thermal diffusivity is given by

$$\chi_e^{\text{TEM}} = \frac{3}{2} D_t \left(\frac{R}{L_{Te}}\right). \quad (8)$$

The non linear dynamics of the TEM mode transfers energy from low $k_y \rho_s \ll 1$ to high $k_y \rho_s$ [21].

3. Eigenmode spectrum of fluctuations

In order to understand the nonlinear dynamics of the system, it is useful to first understand the linear eigenmode spectrum. The linearized dimensionless equation for $y_k^T := (\varphi_k, A_k, T_k)$ can be written compactly as follows:

$$M_k \frac{dy_k}{dt} = L_k y_k, \quad (9)$$

where the matrix M_k is given by

$$M_k = \begin{pmatrix} 1 + k_\perp^2 & 0 & 0 \\ 0 & \frac{\beta}{2} + k_\perp^2 & 0 \\ 0 & 0 & 1 \end{pmatrix} \quad (10)$$

and for ETG modes the components of the matrix L_k are given by

$$\begin{aligned} L_{11} &= ik_y [1 - 2\epsilon_n - (1 + \eta_e) k_\perp^2] - \mu k_\perp^4, \\ L_{12} &= -ik_z k_\perp^2, \\ L_{13} &= ik_y \epsilon_n, \\ L_{21} &= -2ik_z, \\ L_{22} &= -i \frac{k_y \beta}{2} (1 + \eta_e) - k_\perp^2 \left(\frac{\eta}{\mu_0}\right), \\ L_{23} &= ik_z, \\ L_{31} &= -ik_y [\eta_e - 4\epsilon_n (\Gamma - 1)], \\ L_{32} &= ik_z (\Gamma - 1) k_\perp^2, \\ L_{33} &= -2ik_y \epsilon_n (2\Gamma - 1) - k_\perp^2 \chi_\perp. \end{aligned} \quad (11)$$

The ratio of the specific heats, Γ , is chosen to be 1, 5/3 or 2 corresponding to isothermal, three-dimensional adiabatic and two-dimensional adiabatic electron fluids, respectively. Gyrokinetic equations eliminate Γ . The eigenvalue problem is solved numerically for $k = (k_y, k_z)$ at each radius r , e.g. for NSTX $r = 0.6$ m, where the parameter values are $\epsilon_n = 0.18$, $\eta = 1.70$, $\beta = 0.0052$, $\Gamma = 5/3$, $\mu = 1 \times 10^{-4}$, $\chi = 1 \times 10^{-4}$ and $\eta/\mu_0 = 1 \times 10^{-4}$. The results show a wide range of ETG turbulence in both tokamaks. Figure 8 shows the three branches of frequency and growth rate as a function of the normalized wave vector \mathbf{k} , for the given parameters. We see that for $k_y, k_z \gg 1$, the system is linearly stable. In figure 9, we show a cut of the previous surface plots by the

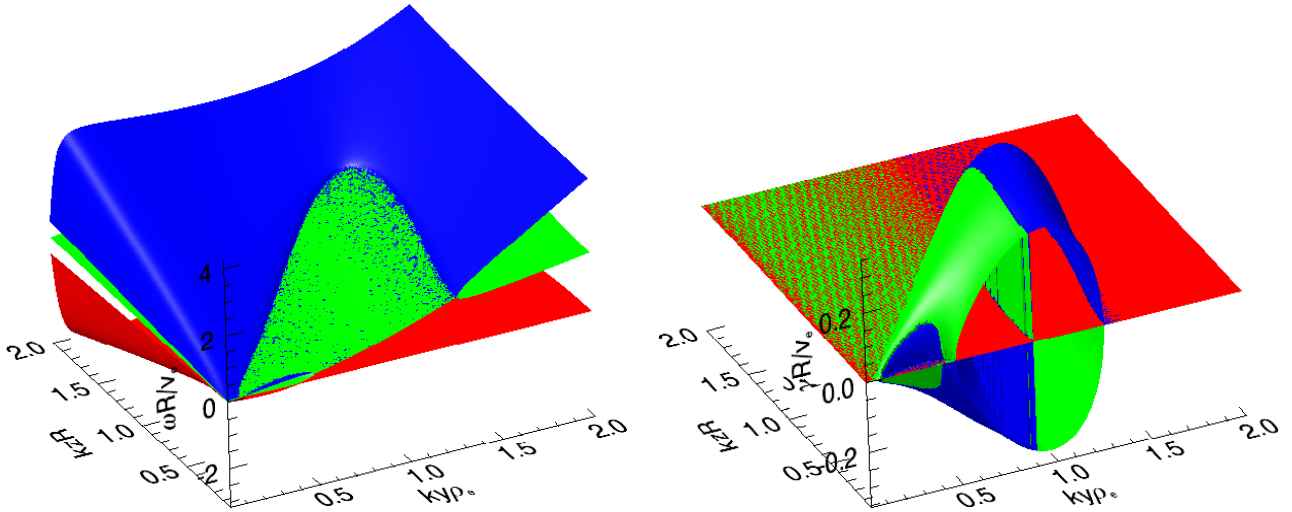


Figure 8. Dispersion relation $\omega = \omega(\mathbf{k})$ on the left and $\gamma = \gamma(\mathbf{k})$ in units of v_e/R on the right. The k_y, k_z wavenumbers are normalized by $k_y \rho_e$ and $k_z R$.

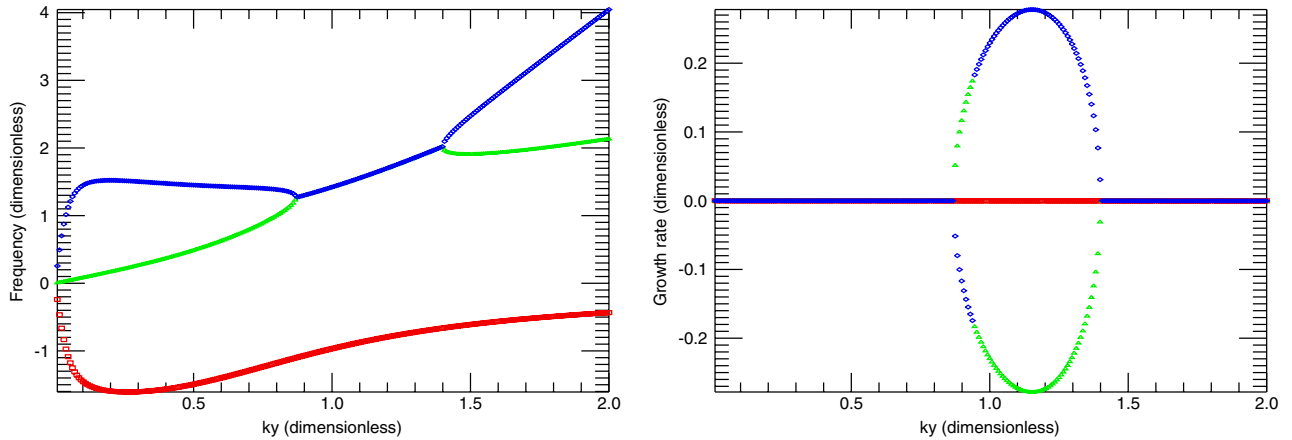


Figure 9. Dispersion relation $\omega = \omega(k_y \rho_e, k_z R = 1)$ on the left and $\gamma = \gamma(k_y \rho_e, k_z R = 1)$ on the right. Same units in figure 8.

plane $k_z R = 1$. Other matrices describe the well-known TEM instability, but we will not describe them here.

4. Comparison with electrostatic models and the TEM

If the magnetic vector potential is dropped, the eigenvalue problem is reduced to two equations, one for the vorticity (or charge conservation) equation and one that describes the electron thermal balance. The dispersion relation for this case is a quadratic equation that describes the local toroidal ballooning electron interchange mode. The maximum growth rate occurs for $k_y^{\max} = [(1 - 2\epsilon_n)/(1 + \eta_e)]^{1/2}$ and scales as $\gamma_{\max} = (v_e/R)(\eta_e - \eta_c)^{1/2}$, where η_c is the critical gradient. The quasi-two-dimensional $\varphi_k - T_k$ turbulence grows up and drives the electromagnetic turbulence. Thus, the ETG can be viewed as a source that drives a heat engine working on the plasma, whose output drives thermal transport and the creation of small scale turbulent magnetic fields [22]. Magnetic turbulence with the appropriate character measured in TS [23–25] was originally thought to be the source of the

large χ_e transport. The response of the short wavelength ETG type of fluctuations to changes in the ETG, when modulated with ECE heating pulses, has been indentified in DIII-D with a new array of electromagnetic scattering experiments extending to 40 cm^{-1} [17].

The short wavelength turbulence couples to the long wavelength turbulence that is also driven independently by the ballooning mode in the bounce averaged grad- B /curvature guiding centre drifts. Here, however, only the trapped electrons contribute, so the mode is named the trapped electron mode or TEM. While the turbulence on this scale length adds to the overall electron heat flux, it is not as fundamental or as universal in nature as that on the electron space and time scales. The TEM mode, known from the early 1970s, has several well-known difficulties in explaining electron transport: (1) the radial profiles of χ_e and the associated heat flux are strongly decreasing functions of minor radius; (2) there is no clear ETG threshold in the model, but instead the model gives a critical gradient for the ITG and can readily exist with zero ETG; (3) the turbulence level is sensitive to the fraction of trapped electrons and weak in machines and radii where the trapped fraction is low; (4) there is

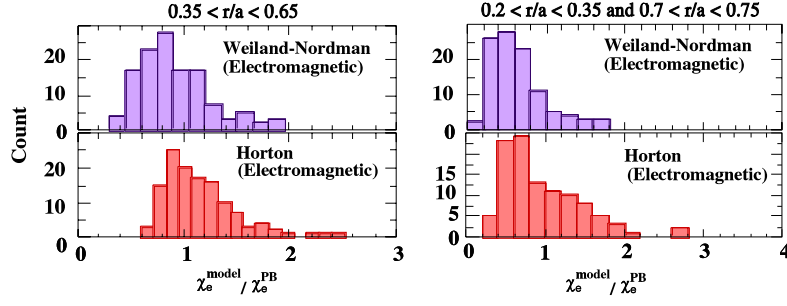


Figure 10. Comparison of the probability distribution of the ratio of the model electron diffusivity to the power balance diffusivity for a sample of 252 data points (12 radial position \times 21 time slice in 8 discharges). The data covers the parameters range of $T_e = 0.3\text{--}5.5$ keV and $n_e = 2.5\text{--}6.5 \times 10^{19} \text{ m}^{-3}$ with $q = 1.1\text{--}4.5$. The data is obtained in TS with fast wave electron heating power from 0.75 to 7.4 MW. Adjustments were made to the Weiland–Nordman model (lowering k_{y,ρ_s} to fit χ_e^{PB}) to obtain this comparable pdf for the TEM–ITG model.

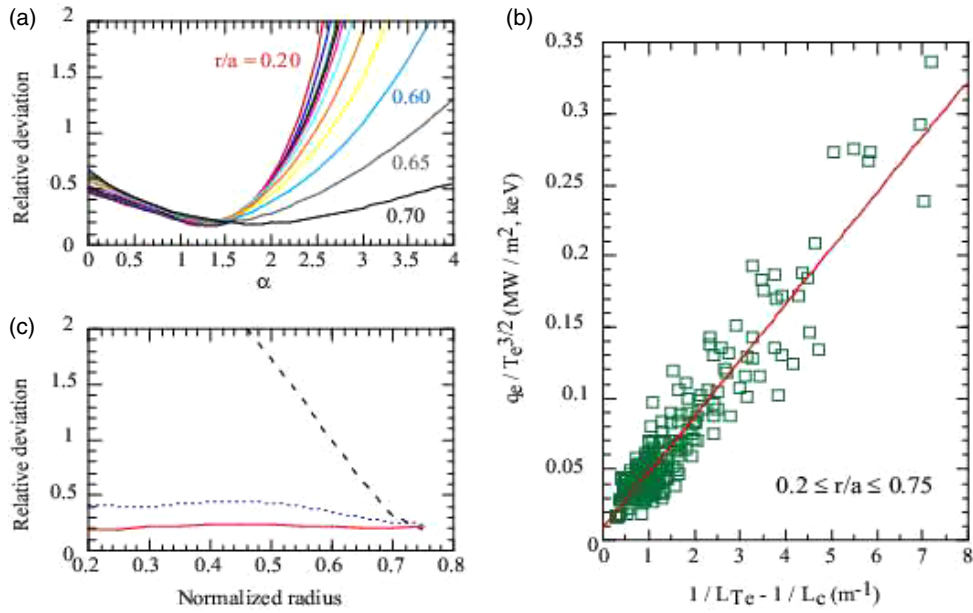


Figure 11. The scaling exponents of temperature and density for the model heat flux versus the experimental heat flux: (a) gives the optimal exponent $\alpha = 1.5$ for the T_e dependence, (b) shows the well-defined critical gradient of the thermal flux scaled by $T_e^{3/2}$ versus the temperature gradient for a large number of shots in TS and (c) shows the relative deviation of the heat flux normalized to $T_e^{3/2}$ (—) compared with $n_e T_e^{5/2}$ (- - -) and $n_e T_e^{3/2}$ (⋯⋯).

no intrinsic magnetic flutter with the mode and, in fact, increasing the plasma pressure measured by the MHD $\alpha = -q^2 R \mu_0 dp / B_T^2 dr$ stabilizes the mode through a subtle effect involving the geodesic component of the magnetic curvature vector and the radial wave number of the eigenmodes; (5) the use of the χ_e^{TEM} formulae in predictive transport code simulations produces profiles in poor agreement with the experimental data and, when used in globally integrated modelling, produces a global energy confinement law that disagrees with the global ITER database confinement laws. By having ETG as the primary source of the electron transport and the TEM as a secondary or supplemental mechanism, the interpretative codes give the observed properties of the electron transport.

In figure 10 we construct the probability distribution for the ratio $x = \chi_e^{\text{model}} / \chi_e^{\text{PB}}$ for the Weiland–Nordman electromagnetic TEM–ITG model in the upper panel and the Horton ETG model in the lower panel. The electrostatic version of the TEM–ITG model gave too wide a distribution

to be compared with the results shown in figure 10. To use the Weiland–Nordman model, the value of k_{y,ρ_s} in the model had to be lowered from 0.3 to 0.03 to obtain the value shown in figure 10. Both models show a skewed distribution with an excess of high value of $\chi_e^{\text{model}} / \chi_e^{\text{PB}}$.

Figure 11 shows the transport scaling $q \sim n^\beta T^\alpha$, which shows the preferred exponents α and β consistent with ETG transport. Figure 11(a) shows the relative deviation of the model from the data for the exponent α in the heat flux, with clear minimum near $\alpha = 3/2$ equivalent to $\chi_e \sim T_e^{1/2}$. Figure 11(b) shows the well-defined relation between the heat flux scaled by $T_e^{3/2}$ and $1/L_{Te} - 1/L_{Te,\text{crit}}$ for a wide range of data points over many discharges and positions within a single discharge. Figure 11(c) shows quantitatively the relative deviation of the normalized heat flux for the electromagnetic scaling of $q_e \sim T_e^{3/2}$ (solid line) along the radial positions which is small and uniform at 20% compared with two electrostatic scalings $q_e / (n T_e^{3/2})$ (dotted line) and $q_e / (n T_e^{5/2})$ (dashed line) for the ITG–TEM mode.

For the 10 MW upgraded TS experiments, currently being performed, the ETG scaling in figure 11 predicts the central temperature reaches 9–10 keV.

5. Conclusions and discussion

Transport analysis of TS and NSTX discharges, with centrally deposited fast wave electron heating, leads to the conclusion that the ETG instability provides a reliable baseline model for electron transport. Measurements of the electron temperature and density profiles, combined with results from fast wave RF computations for the power deposition, allow detailed interpretation of the electron thermal flux versus temperature gradient. Evidence supporting ETG turbulent transport in these two confinement devices includes: (1) a consistent scaling in density and temperature, both in the profiles and the parametric variations, (2) a clear analytical and fundamental thermodynamic origin for the critical temperature gradient and its dependence on magnetic shear [3], (3) the turbulence is not particularly sensitive to the mixture of trapped and passing electrons [4], (4) the turbulence generates self-consistently a magnetic flutter component from the parallel electron currents [26] and (5) thermal flux formulae used in radial transport codes with auxiliary heating give good agreement with the measured profiles, both in radius and in time.

The high grade confinement in the reversed shear, high beta spherical tokamak can be understood from the following flux, gradient and plasma parameters. In the ITB NSTX discharge (#105830), the maximum ETG is 10.9 keV m^{-1} at $r/R = 0.24$, where $n_e = 1.5 \times 10^{19} \text{ m}^{-3}$ and $T_e = 2.5 \text{ keV}$, and thus $v_{*e} n_e T_e = 45 \text{ MW m}^{-2}$. Here v_{*e} is the electron diamagnetic drift velocity. From the actual power balance, the thermal flux is $q_e^{\text{PB}} = 0.17 \text{ MW m}^{-2}$ and the local thermal diffusivity is $\chi_e = q_e^{\text{PB}} / (-n_e (dT_e/dr)) = 6.43 \text{ m}^2 \text{ s}^{-1}$. For reference, the Bohm diffusivity $T_e/16eB$ is $349 \text{ m}^2 \text{ s}^{-1}$ which is larger by a factor of 54. This reduction of electron transport from the Bohm value is a record for sub-mega-ampere tokamaks with 4 keV core temperature.

An interpretative simulation with ETG for TS is shown in figure 1 using the CRONOS integrated transport code [5] with a stair-stepped fast wave heating profile of 3 and 6 MW. A NSTX HHFW heated discharge with $T_{e0} = 4 \text{ keV}$ shows electron transport that is explained by the ETG model. Finally, we can explain how the weakly reversed magnetic shear profiles produced in optimized NSTX/HHFW discharges and fast current ramp TS discharges partially block the transport of electron guiding centres because of the formation of a shearless invariant curve in the corresponding drift wave transport model. Weakly reversed magnetic shear discharges in NSTX are accompanied by global electron transport that is reduced by half, with an associated increase of impurity ions due to an inward electric field. Explanations based on the general principles of dynamical systems are offered for these enhanced electron confinement regimes.

Acknowledgments

This work is supported under the US Department of Energy contract DE-FG02-04ER-54742, the Association Euratom-CEA, CEA/DSM/DRFC CEA France and the Department of

Controlled Fusion Research in Commissaire Energy Agency France as well as by the Australian Research Council.

Appendix. The drift kinetic electron model

The dynamical equations using the linearized drift kinetic equation to close the moment equations have been obtained. This closure removes the need to given an *ad hoc* specification of the adiabatic gas constant in the electron pressure equation.

To describe the ETG electron dynamics without the fluid closure in the PDEs equations (A1)–(A10), we use the drift-kinetic theory. Here we introduce the single particle phase space density $F(x_i, v_{\parallel}, \mu, t)$ with the guiding centre orbits for the electrons in a covariant description of the confinement geometry. For the geometry, we use $B_i = B b_i$ where ($b_i b_i = 1$) B is the field strength and b_i is the unit vector. To simplify the presentation, we ignore the magnetic field gradient and curvature drift and retain only the polarization drift in $\dot{X}_i^{(1)}$. The second order $\dot{X}_i^{(2)}$ describes the finite Larmor radius correction to the guiding centre orbit and involves the cross-field dyadic $I_{ij} = \delta_{ij} - b_i b_j$.

The drift-kinetic equation is

$$\frac{1}{B} \frac{\partial}{\partial t} (BF) + \frac{1}{B} \frac{\partial}{\partial x_i} (B \dot{X}_i F) + \frac{1}{B} \frac{\partial}{\partial v_{\parallel}} (B \dot{V}_{\parallel} F) + \frac{1}{B} \frac{\partial}{\partial \mu} (B \dot{\mu} F) = 0. \quad (\text{A1})$$

The dynamics of the guiding centre orbits are

$$\dot{X}_i = \dot{X}_i^{(0)} + \dot{X}_i^{(1)} + \dot{X}_i^{(2)}, \quad (\text{A2})$$

$$\dot{X}_i^{(0)} = V_{\parallel} b_i + V_{Ei}, \quad (\text{A3})$$

$$\dot{X}_i^{(1)} = \frac{\epsilon_{ipq} b_p}{\Omega} \frac{\partial V_{Eq}}{\partial t}, \quad (\text{A4})$$

$$\dot{X}_i^{(2)} = \frac{\mu B}{m \Omega^2} \left(\frac{\partial}{\partial x_j} I_{ij} \frac{\partial V_{Ei}}{\partial x_k} - \frac{\partial}{\partial x_j} I_{ik} \frac{\partial V_{Ej}}{\partial x_k} \right), \quad (\text{A5})$$

$$\dot{V}_{\parallel}^{(0)} = \frac{e}{m} b_i E_i - \frac{\mu}{m} b_i \frac{\partial B}{\partial x_i} - b_i \frac{D V_{Ei}}{D t} \quad (\text{A6})$$

$$\dot{V}_{\parallel}^{(1)} = 0, \quad (\text{A7})$$

$$\dot{V}_{\parallel}^{(2)} = 0, \quad (\text{A8})$$

$$\dot{\mu}^{(0)} = -\frac{\mu}{B} \left(\frac{\partial B}{\partial t} + V_E \cdot \nabla B + B \nabla_{\perp} \cdot V_E \right), \quad (\text{A9})$$

$$\dot{\mu}^{(1)} = -\frac{\mu}{B} \frac{\partial}{\partial x_i} \left(B \frac{\epsilon_{ipq} b_p}{\Omega} \frac{\partial V_{Eq}}{\partial t} \right), \quad (\text{A10})$$

where

$$\frac{D V_{Ei}}{D t} = \frac{\partial V_{Ei}}{\partial t} + (V_{\parallel} b + V_E) \cdot \nabla V_{Ei}.$$

The orbits in equations (A2)–(A10) satisfy

$$\frac{1}{B} \frac{\partial}{\partial t} B + \frac{1}{B} \frac{\partial}{\partial x_i} B \dot{X}_i + \frac{1}{B} \frac{\partial}{\partial v_{\parallel}} B \dot{V}_{\parallel} + \frac{1}{B} \frac{\partial}{\partial \mu} B \dot{\mu} = 0. \quad (\text{A11})$$

Then the first moments of equation (A1) are

$$\frac{\partial N}{\partial t} + \frac{\partial}{\partial x_i} N(u_{\parallel} b_i + V_{Ei} + u_{\perp i}) = 0 \quad (\text{A12})$$

$$\begin{aligned} N \frac{\partial u_{\parallel}}{\partial t} + N(u_{\parallel} b_i + V_{Ei} + u_{\perp i}) \frac{\partial u_{\parallel}}{\partial x_i} + \frac{\partial}{\partial x_i} \frac{P_{\parallel}}{m} b_i - \frac{Ne}{m} E_{\parallel} \\ + \frac{P_{\perp}}{mB} b \cdot \nabla B + Nb \cdot \frac{DV_E}{Dt} + \frac{\partial}{\partial x_i} \int d^3 v F(v_{\parallel} - u_{\parallel}) \\ \times \frac{\mu B}{m\Omega^2} \frac{\partial}{\partial x_j} \left(I_{jk} \frac{\partial V_{Ei}}{\partial x_k} - I_{ik} \frac{\partial V_{Ej}}{\partial x_k} \right) = 0 \end{aligned} \quad (\text{A13})$$

$$\begin{aligned} \frac{\partial P_{\parallel}}{\partial t} + \frac{\partial}{\partial x_i} P_{\parallel}(u_{\parallel} b_i + V_{Ei}) + 2P_{\parallel} \left(b_i \frac{\partial u_{\parallel}}{\partial x_i} - V_{Ei} k_i \right) \\ + 2b_i \frac{\partial B}{\partial x_i} \int d^3 v F \mu (v_{\parallel} - u_{\parallel}) \\ + \frac{\partial}{\partial x_i} m b_i \int d^3 v F (v_{\parallel} - u_{\parallel})^3 = 0, \end{aligned} \quad (\text{A14})$$

$$\begin{aligned} \frac{\partial P_{\perp}}{\partial t} + \frac{\partial}{\partial x_i} P_{\perp}(u_{\parallel} b_i + V_{Ei}) + P_{\perp} \left(\frac{\partial V_{Ei}}{\partial x_i} + u_{\parallel} \frac{\partial b_i}{\partial x_i} + V_{Ei} k_i \right) \\ + \frac{\partial}{\partial x_i} b_i \int d^3 v F \mu (v_{\parallel} - u_{\parallel}) = 0, \end{aligned} \quad (\text{A15})$$

where

$$u_{\perp i} = \frac{1}{\Omega} \epsilon_{ipq} b_p \frac{\partial V_{Eq}}{\partial t} + \frac{P_{\perp}}{Nm\Omega^2} \frac{\partial}{\partial x_j} \left(I_{jk} \frac{\partial V_{Ei}}{\partial x_k} - I_{ik} \frac{\partial V_{Ej}}{\partial x_k} \right).$$

Equations (A12)–(A15) are a new formulation for the electron dynamics, with a closure based on neglect of the divergence of the guiding centre thermal flux. The fifth order polynomial dispersion relation may be compared with the linear nonlocal dispersion relation derived from equation (1).

References

- [1] Kadomtsev B.B. 1992 *Tokamak Plasmas: A Complex Physical System* (Bristol: Institute of Physics Publishing) pp 124–50
- [2] Hoang G.T., Bourdelle C., Garbet X., Giruzzi G., Aniel T., Ottaviani M., Horton W., Zhu P. and Budny R. 2001 *Phys. Rev. Lett.* **87** 125001
- [3] Hoang G.T., Horton W., Bourdelle C., Hu B., Garbet X. and Ottaviani M. 2003 *Phys. Plasmas* **10** 405
- [4] Horton W., Hoang G.T., Bourdelle C., Garbet X., Ottaviani M. and Colas L. 2004 *Phys. Plasmas* **11** 2600
- [5] Basiuk V. *et al* 2003 *Nucl. Fusion* **43** 822–30
- [6] LeBlanc B.P. *et al* 2004 *Nucl. Fusion* **44** 513–23
- [7] Hoang G.G. *et al* 2000 *Phys. Rev. Lett.* **84** 4593
- [8] Kwon J.M., Horton W., Zhu P., Morrison P.J., Park H.B. and Choi D.I. 2000 *Phys. Plasmas* **7** 1169
- [9] del Castillo-Negrete D. and Morrison P.J. 1993 *Phys. Fluids A* **5** 948
- [10] Greene J.M. 1979 *J. Math. Phys.* **20** 1183
- [11] Finn J.M. 1975 *Nucl. Fusion* **15** 845–54
- [12] Wurm A., Apte A., Fuchss K. and Morrison P.J. 2005 *Chaos* **15** 023108
- [13] Apte A., Wurm A. and Morrison P.J. 2003 *Chaos* **13** 421
- [14] Apte A., Wurm A. and Morrison P.J. 2004 Separatrix reconnection and meanders in the standard nontwist map *Proc. 2004 International Sherwood Fusion Theory Conf. (Missoula, Montana, 26–28 April 2004)*
- [15] Corso G. and Prado S.D. 2003 *Chaos Solitons Fractals* **16** 53–7
- [16] Petrisor E., Misguich J.H. and Constantinescu D. 2003 *Chaos Solitons Fractals* **18** 1085–99
- [17] Peebles W.A. 2005 First observation of low, intermediate and high k turbulence in DIII-D *Invited Talk at DDP-APS (Savannah, GA)*
- [18] Ongena J., Evrard M. and McCune D. 1998 *Trans. Fusion Technol.* **33** 181–91
- [19] Horton W. 1986 *Phys. Fluids* **29** 1491
- [20] Horton W. and Ichikawa Y.-H. 1997 *Chaos and Structures in Nonlinear Plasmas* (Singapore: World Scientific) chapter 7, p 225
- [21] Kadomtsev B.B. and Pogutse O.P. 1970 *Reviews of Plasma Physics* (New York: Consultants Bureau) chapter 2, p 380
- [22] Holland C. and Diamond P.H. 2004 *Phys. Plasmas* **11** 1043
- [23] Zou X.L., Colas L., Paume M., Chareau J.M., Laurent L., Devynck P. and Gresillon D. 1995 *Phys. Rev. Lett.* **75** 1090
- [24] Devynck P. *et al* 1997 *Plasma Phys. Control. Fusion* **39** 1355
- [25] Colas L. *et al* 1998 *Nucl. Fusion* **38** 903
- [26] Wong K.L., Itoh K., Itoh S.I., Fukuyama A. and Yagi M. 2000 *Phys. Lett. A* **276** 281–5